Dynamic models for power transmission monitoring in non-stationary conditions based on IAS signals

Nathanael Thibault, Adeline Bourdon, Didier Rémond, Damien Lecouvreur

Mechanism and Machine Theory 201 (2024) 105733

Contents lists available at ScienceDirect

Mechanism and Machine Theory

journal homepage: www.elsevier.com/locate/mechmt

Research paper

Dynamic models for power transmission monitoring in non-stationary conditions based on IAS signals

Nathanael THIBAULT [a,b], Adeline BOURDON [a], Didier RÉMOND [a,*], Damien LECOUVREUR [b]

[a] INSA Lyon, CNRS, LaMCoS, UMR5259, 69621 Villeurbanne, France
[b] Safran Helicopter Engines, Avenue Szydlowski, 64511 Bordes, France

ARTICLE INFO

Keywords:
Non stationary conditions
Mechanical model
Dynamics
Gear
Bearing
Fault monitoring

ABSTRACT

This paper describes a dynamic model of two stage gear power transmission including shafts, ball and roller bearings as well as spur and helical gears. The fundamental objective of this model is to introduce a simulator of realistic signals for monitoring the dynamic behavior of such transmissions in non-stationary operating conditions. Special attention is paid to the couplings between mechanical components through the shaft rotation. The analyses carried out are mainly based on the Instantaneous Angular Speed (IAS) as an alternative signal to classical vibrations. Simulations have demonstrated the relevance of IAS as a tool for health monitoring of common gear or bearing faults in non-stationary operating conditions. Suggested angular approaches offer the ability to separate excitations from the transfer function of the system. The interactions between bearings and gears appear as modulation sidebands and suggest a new way to use demodulation methods. Finally, the influence and the detectability of damages on both mechanical components (spall on bearings, spall and crack on gears) using the mentioned techniques are discussed, offering new incomes for signal processing tools in gear transmission monitoring.

1. Introduction

Gear power transmissions are central and key elements for numerous systems in various domains as transportation, energy production, manufacturing or machining. Their failures are usually critical and are causes of operation interruptions or even damages for the whole system. Thus, it is important to detect and localize a damage as early as possible. Moreover, next power transmission generations will operate in non-stationary conditions mainly with the electrification of transportation. For this purpose, the knowledge of the failure modes and their influence on the system dynamic behavior is fundamentally required for robust monitoring tools. Mechanical models are then needed and useful to predict healthy and damaged system dynamics in order to be able to detect fault on real systems and to understand their manifestations in various operating conditions.

Rotating machinery monitoring is usually performed using accelerometric data and the literature is extensive on this topic with a strong insight about signal processing methods. Generally, well designed for stationary conditions these signal processing tools are built on signal models with low complexity and weak connections to kinematics and dynamics of the transmission. However, this paper focuses on the Instantaneous Angular Speed (IAS) signal because of its relevance in case of non-stationary operating conditions [1]. Its measurement method implies a natural angular sampling which is best suited for the monitoring of discrete periodic components in

* Corresponding author.

https://doi.org/10.1016/j.mechmachtheory.2024.105733
Received 12 February 2024; Received in revised form 20 June 2024; Accepted 5 July 2024

rotation like bearings, gears or electrical rotors. The IAS signal may be obtained by measuring the time duration (number of clock ticks) between two successive events provided by an optical encoder signal. The IAS signal is then sampled with a constant step of the reference shaft given by the encoder resolution and is expressed as:

$$IAS(i\Delta\theta) = \frac{\Delta\theta}{\Delta t_i} = \frac{2\pi}{R}\frac{f_c}{N_i} \tag{1}$$

With R being the encoder resolution, f_c the clock frequency and N_i the number of clock ticks between shaft positions $(i-1)\Delta\theta$ and $i\Delta\theta$.

Moreover, IAS perturbations generated by bearings and gears have been proved to be easily transmitted through connecting elements and the whole transmission is possible to monitor using a single sensor. IAS has been firstly studied while measuring Transmission Error in automotive gearboxes [2] and remains strongly related to the kinematics of the transmission.

Gear modeling has been a subject of interest for several decades and numerous models of variable complexity have been proposed. The more precise ones are based on numerical methods such as Finite Elements (FE) [3] [4],. Other authors have developed hybrid models [5] [6], combining numerical and analytical approaches for structural and contact deflection respectively. These models require significant computation time and are less suitable for dynamic simulations, particularly for non-stationary conditions. In this paper, a fully analytical model is preferred to FEM approaches in order to be consistent with non-stationary conditions and to keep affordable computing time for long simulations. The model is similar to classical meshing stiffness calculations but introduces forces acting on the different components of the transmission. One of the first works on mesh stiffness calculation was performed by Weber [7] and then improved with Banaschek [8]. It adopts a non-uniform cantilever beam model for the gear teeth. The stiffness calculation considers the deflection associated to the beam, the contact and the foundation as a semi-infinite elastic plane. This work has been used and modified by numerous author like Attia [9] to extend it to thin rimmed gears or then by Cornell [10] and later by Sainsot & al. [11] regarding the foundation stiffness calculation. The works from Chen & al. [12] [13], and Chaari & al. [14] have introduced a tooth root crack and Mohammed & al. [15] have improved the estimation of a damaged tooth stiffness. In parallel, Tse & al. [16] have implemented off-line-of-action contacts, the influence of which on the Static Transmission Error (STE) and on the dynamic behavior was highlighted by Lin & al. [17] and Singh & al. [18].

A first part of this paper describes the model of a transmission and goes into gear model details. Special attention is given to implementation of the complete geometry of teeth and on the introduction of damage. The bearing model has been detailed and discussed in a previous publication [19] and is extended to the case of cylindrical roller bearings. The second part of this paper is dedicated to the numerical study of the behavior of an academic power transmission operating under non-stationary conditions. The two-stage power transmission is composed by three flexible shafts, each of them supported by ball and roller bearings and linked by spur and helical gear pairs. The strong coupling intrinsic to the modeling method allows the study of gear-bearing interactions and their benefits in health monitoring. The relevance of IAS as a monitoring tool and the benefits of non-stationary conditions are also highlighted through the richness of signal components. Finally, the influence of damages like spalls for bearings and spalls or cracks for gears on the IAS is analyzed and discussed through numerical experiments.

2. Rotating assembly model introduction

2.1. Modeling principle

The modeling of the flexible shafts is assumed by using Timoshenko beam elements and leads to the differential system introduced in eq (2) where M and K are the mass and stiffness matrices of the shafts. C is the damping matrix estimated using a classical modal approach with a modal damping coefficient set to 0.01. Finally, $X^t = \{X_1, X_2, \ldots, X_n\}$ is the state vector of the system with $X_i = \{x_i,\ y_i,\ z_i,\ \theta_{xi},\ \theta_{yi},\ \theta_{zi}\}$ being the translation and rotation displacements of node i. In the presented model, no assumption is made on the rotating speed and θ_z is the complete rotation degree of freedom, including the rigid body rotation and not limited to torsional effects. In general, this point of attention is rarely considered in conventional models where some degrees of freedom are considered at the same time as only a deformation or a global position, except when the models strongly need to take account of relative angular positions like for planetary gear sets [20]. Indeed, and specially for non-stationary conditions, the absolute angular position of the shaft is of first importance and leads to strong couplings associated with shaft rotation in the dynamic model [21].

$$M\ddot{X} + C\dot{X} + KX = F_{ext}(t) \tag{2}$$

Bearings are then added as connecting forces acting on two nodes corresponding to their inner ring (IR) and their outer ring (OR) respectively. In a similar way, gears are introduced as connecting forces acting on the nodes associated to the center of the wheels. The use of connecting force vectors for gears and bearings allows a strong coupling between these two kinds of elements. Moreover, it does not require any linearization around an operating point and is particularly suitable for the investigation of non-stationary operating conditions. The mass matrix has been then completed to take account for the mass and inertia of rigid discs standing for the wheels of the gears. Eq. (3) introduces the whole differential system to integrate taking account of gear and bearing connecting forces $F_b\left(X, \dot{X}, \ddot{X}\right)$ for bearings and $F_g(X, \dot{X})$ for gears described in the following sections. Unlike external forces, these connecting forces depend on the displacements of nodes and their derivatives rather than time.

$$M\ddot{X} + C\dot{X} + KX = F_{ext}(t) + F_b\left(X, \dot{X}, \ddot{X}\right) + F_g(X, \dot{X}) \tag{3}$$

The calculation of ball bearing forces is performed using the model proposed by Thibault & al. [19]. The model used for roller bearings is similar and the only difference lies in the expressions of forces acting on the rolling elements. The contact between rollers and races is of type cylinder-cylinder and the contact on flanges has to be considered to ensure stability. The model of roller bearings is based on the works of Bourdon [22] and Hamrock & al. [23]. The calculation of the gear forces is detailed in the following sections.

2.2. Mesh deflection

The gear mesh model is dedicated to the calculation of dynamic forces transmitted and not to the design and calculation of gear geometry. It is therefore important to limit computation time while assuring correct estimation of contacting forces. For this purpose, an analytical model is adopted. It takes as input the translational and rotational displacements $\left(x_i, y_i, z_i, \theta_{xi}, \theta_{yi}, \theta_{zi}\right)$ of the nodes associated to the center of both wheels and return the connecting forces applied to these nodes. The wheel node displacements allow an estimation of the tooth deformation from which one can estimate the corresponding force which should be applied to reach this deformation. The contacting forces are then computed separately on each tooth pair. In order to easily take account of helix angle and potential non-uniform damages along the tooth width, these are discretized as K thin slices in the axial or helical direction as shown in Fig. 1 [11,13-15]. The calculation of deflection is done separately on each slice. In the following, the index $j \in [1:Z]$ stands for the tooth considered while the index $k \in [1:K]$ corresponds to the slice.

Without load or profile modification, the contact point P_{jk} between two slices moves on the line of action during the rotation of wheels. The contact exists for a rotation equal to the driving angle. The tooth or slice deflection at the contact point is calculated kinematically. For this purpose, the displacement of both wheels at the contact point are calculated separately. Since the principal rotation degree of freedom stands for the complete rotation, it has to be considered differently. Let $\Delta\theta_z = \theta_{z20} + \frac{Z_1}{Z_2}\theta_{z10}$ be the Transmission Error, O_i the center of wheel i and $R_\Delta(\phi)$ the rotation matrix of angle ϕ around the axis $\Delta = x,y,z$. We can then calculate the displacement of both wheels as follows:

$$\begin{aligned} \overrightarrow{d_{ijk}} &= \begin{pmatrix} x_i \\ y_i \\ z_i \end{pmatrix} + \left[R_x(\theta_{xi}) + R_y\left(\theta_{yi}\right) \ - 2.Id_3\right] \cdot \overrightarrow{O_iP_{jk}} \ i = 1,2 \\ \overrightarrow{d_{\theta z,jk}} &= \left(R_z(\Delta\theta_z) - Id_3\right) \cdot \overrightarrow{O_2P_{jk}} \end{aligned} \tag{4}$$

The total deflection is then:

$$\delta_{jk} = \left(\overrightarrow{d_{1jk}} - \overrightarrow{d_{2jk}} - \overrightarrow{d_{\theta z,jk}}\right) \cdot \vec{n} \tag{5}$$

Here, $\vec{n}$ is the normal vector to the tooth profile and Id_3 is the identity matrix. All the stiffness and deformation are also estimated with a corrective term which is introduced if the adjacent slices are unloaded. This correction is dedicated to the introduction of convective effects on flexion. The corrective term is defined for the unloaded slices corresponding to a given length and is defined by a comparison with a dedicated Finite Element model.

2.3. Contact force

The total deflection previously calculated is the sum of tooth deflection, contact deflection and fillet-foundation deflection. Tooth stiffness is determined using the expression given by Chen & al. [12,13] who assume it to behave as a cantilever beam accounting for

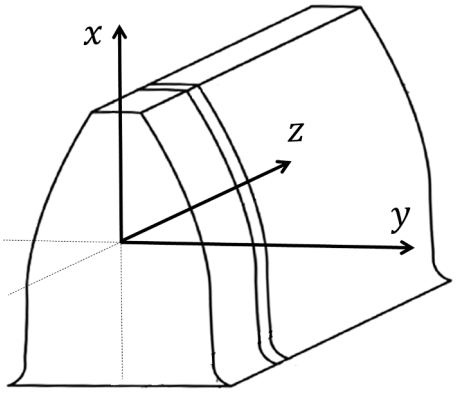

Fig. 1. Tooth discretization in axial or helical direction.

bending, shear and compression. Fig. 2 shows a schema of a tooth under load. Eq. (6) gives formulae of the tooth stiffness for each deformation mode obtained using the potential energy stored in the tooth. Here, G is the shear modulus while A and I are the section area and moment of inertia respectively. Finally, b_{eff} is the angle defining the orientation of the contact force with respect to the bisector of the tooth.

$$\frac{1}{K_b} = \int_0^d \frac{\left(x\cos\left(b_{eff}\right) - h_{eff}\sin\left(b_{eff}\right)\right)^2}{EI(x)}dx$$

$$\frac{1}{K_s} = \int_0^d \frac{1.2\cos^2\left(b_{eff}\right)}{GA(x)}dx \tag{6}$$

$$\frac{1}{K_c} = \int_0^d \frac{\sin^2\left(b_{eff}\right)}{EA(x)}dx$$

The fillet-foundation stiffness is calculated as suggested by Sainsot & al. [11] by assimilating the wheel to an elastic disc (see Fig. 2). The expression is given in Eq. (7) where δz is the tooth width and E the Young modulus. The coefficients L^*, M^*, P^*, Q^* are obtained using polynomial regression based on FE results and given in Appendix 3.

$$\frac{1}{K_f} = \frac{\cos^2\left(b_{eff}\right)}{E\delta z}\left[L^*\left(\frac{d}{S_{root}}\right)^2 + M^*\frac{d}{S_{root}} + P^*\left(1 + Q^*\tan^2\left(b_{eff}\right)\right)\right] \tag{7}$$

Several contact laws are found in the literature as the empiric formula of Palmgren [24] or the formula of Lundberg [25]. In this work, the contact deflection is given by Eq. (8) which corresponds to the Johnson law [26] dedicated to cylinder-cylinder contacts. Here, ΔR is the sum of the radii of contacting cylinders, E is the Young's modulus, ν is the Poisson's coefficient and L is the width of the contact zone.

$$\delta_c = \frac{F}{\pi L E^*}\left(\ln\left(\frac{4\pi L E^* \Delta R}{F}\right) - 1\right) \; with \; E^* = \frac{E}{2(1-\nu^2)} \tag{8}$$

The total deflection can then be written as a nonlinear function of the contact force as shown in Eq. (9).

$$\delta_{jk}\left(F_{jk}\right) = F_{jk}\left[\frac{1}{K_{tot}} + \frac{1}{\pi L E^*}\left(\ln\left(\frac{4\pi L E^* \Delta R}{F_{jk}}\right) - 1\right)\right] \tag{9}$$

with:

$$K_{tot} = \left(\frac{1}{K_{b1}} + \frac{1}{K_{s1}} + \frac{1}{K_{c1}} + \frac{1}{K_{f1}} + \frac{1}{K_{b2}} + \frac{1}{K_{s2}} + \frac{1}{K_{c2}} + \frac{1}{K_{f2}}\right)^{-1}$$

By combining this expression with Eq. (4), it is easy to estimate the force applied on each slice.

The main limitations of this model are essentially and deliberately associated with an approximate consideration of the flexibility of

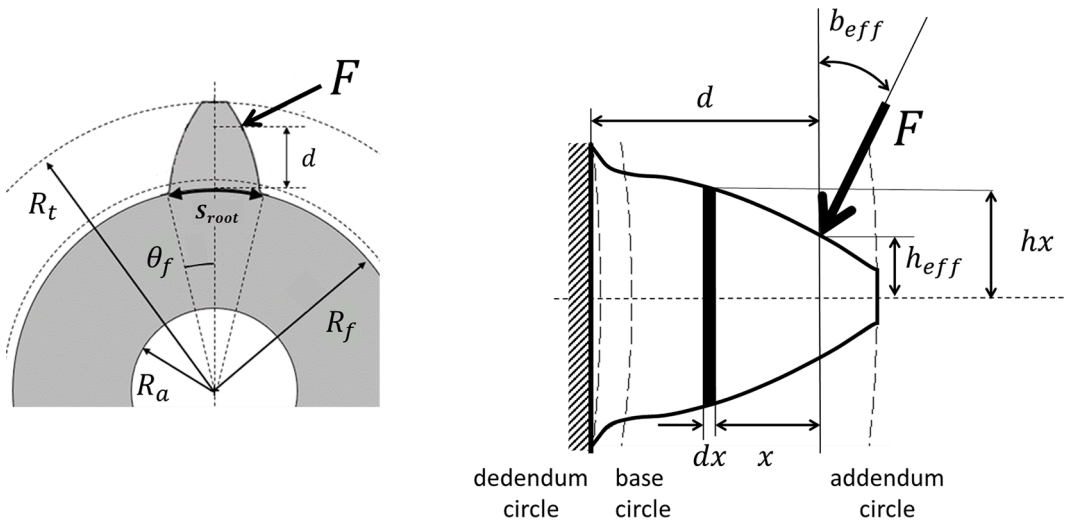

Fig. 2. Schema of a tooth associated to a cantilever beam under load [12].

housing elements and simplified gear geometry. These limitations are not specific to the transmission example chosen and could be easily corrected by introducing other flexible elements. Moreover, no connected device is included in the academic transmission system like turbines or driven machines, corrupting inertia, boundary or load conditions. These improvements would lead to the use of richer, more precise models and make the interactions between excitations and structure more complex. The choice has been made to limit this complexity, which is not required to explain the phenomena highlighted in this paper.

2.4. Energy dissipation

Due to the motion of both wheels, sliding occurs at the contact point. The ensuing tangential force is estimated using the Coulomb law assuming pure sliding. It can be artificially written as $\overrightarrow{F_{t,jk}} = -\mu F_{jk}\,\overrightarrow{t}$ where $\overrightarrow{t} = \frac{\overrightarrow{v_t}}{\|\overrightarrow{v_t}\|}$ and v_t is the tangential part of the relative speed of the bodies. Here, the assumption of pure sliding is a simplification and does not precisely report the contact behavior and the value of μ is equal to 0.03. However, a stick-slip resolution would require too much computation time and is not suitable for this study. The relative tangential speed can be calculated as follows:

$$\overrightarrow{v_t} = (\overrightarrow{v_2} - \overrightarrow{v_1}) - [(\overrightarrow{v_2} - \overrightarrow{v_1}) \cdot \overrightarrow{n}]\,\overrightarrow{n} \qquad with \qquad v_i = \begin{pmatrix} \dot{x}_i \\ \dot{y}_i \\ \dot{z}_i \end{pmatrix} - \overrightarrow{O_iP_{jk}} \wedge \begin{pmatrix} \dot{\theta}_{xi} \\ \dot{\theta}_{yi} \\ \dot{\theta}_{zi} \end{pmatrix} \tag{10}$$

Since the gears are integrated as connecting forces, they are not considered in the computation of the modal damping matrix. Thus, it is required to add a viscous damping force in parallel with the contact force calculated previously and accounting for squeeze-film damping. It can be written as $\overrightarrow{F_v} = -\alpha_{eng} v_n \overrightarrow{n}$ where $v_n = (\overrightarrow{v_2} - \overrightarrow{v_1}).\overrightarrow{n}$ is the normal part of the relative velocity of bodies calculated as previously and $\alpha_{eng} = 100\ N.s.m^{-1}$. Once the deflection and the contact forces are computed on each slice for each tooth pair, the global forces transmitted from one wheel to the other can be obtained by a simple summation.

2.5. Gear mesh model deepening

2.5.1. Off-line-of-action contacts

The kinematic contact zone is defined as the angular zone where contact exists between two teeth from a same pair without load or involute profile modifications. FE results in [5] [27], [28], and analytical results [17] have shown that the limitation of the contact force to kinematic contact zone is not enough to estimate the Static Transmission Error (STE) evolution nor to correctly describe the dynamics of the gears. The limitation to the kinematic contact zone leads to abrupt variations of the mesh stiffness at the entry and the exit of a tooth pair in the contact zone, generating vibrations and IAS variations more important and more impulsive than the real ones. In a more realistic manner the contact between two teeth of a same pair is established progressively before entering in the kinematic contact zone due to Loaded Transmission Error (LTE). The contact point is then not located on the line of action and the direction of the contact force is not given by that. Such contacts are detected by extending the contact research zone upstream and downstream of the theoretical limits. The total deflection outside of the kinematic contact zone is calculated as previously but the separation distance D_{jk} is subtracted:

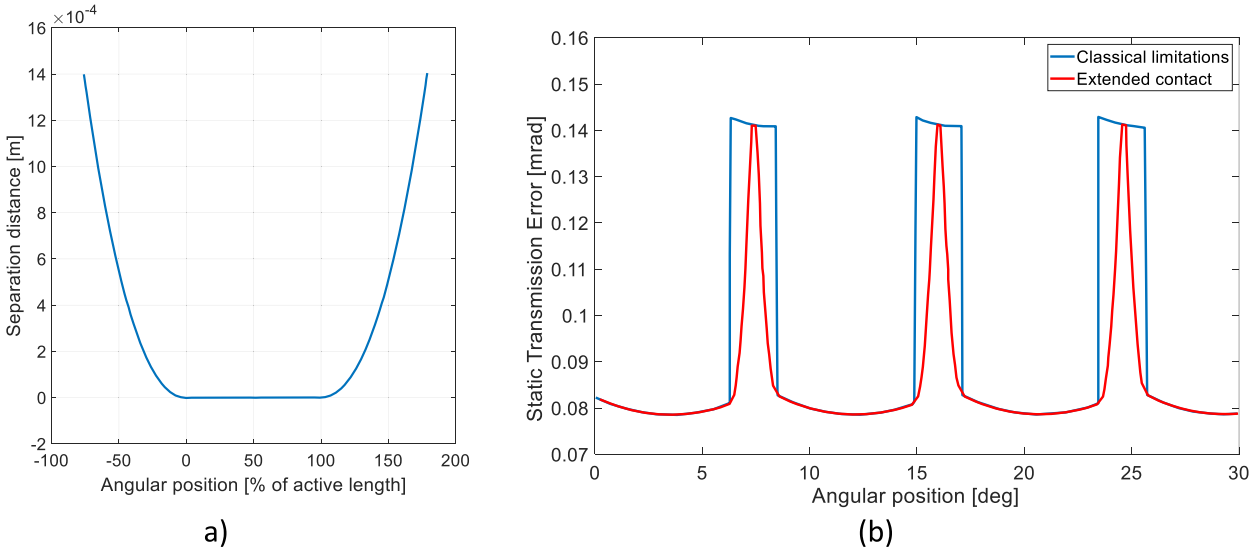

Fig. 3. (a) Separation distance evolution and (b) STE evolution considering classical limitations and off-line-of-action contacts.

$$\delta_{jk} = \left(d_{1jk} - d_{2jk} - d_{\theta z,jk}\right) \cdot \vec{n} - D_{jk} \tag{11}$$

The separation distance is defined as the minimum distance separating the profile of two conjugate teeth when this pair of teeth is not loaded and is obviously extended to conjugate slices. For readability purposes, the calculation of the separation distance, the contact point location and the contact force orientation are not detailed in this paper. However, the method used is similar to the one proposed by Tse & al. [16]. Fig. 3(a) shows the evolution of the separation distance as a function of the angular position expressed as a percentage of the driving angle. By definition, the separation distance is zero for an angular position between 0 and 100 % of the driving angle. It increases rapidly while moving away from this zone. Fig. 3(b) compares the evolution of STE computed with classical limitation and by considering off-line-of-action contacts for a spur gear. Accounting for off-line-of-action contact leads to an increase of the angular domain where two teeth of a same pair remain in contact.

2.5.2. *Tip fillets and profile corrections*

Involute profiles are usually corrected in order to decrease the impact of entry or exit of a tooth pair in the contact zone on the vibrations and on the IAS. These modifications are important to consider in a dynamic model in order to correctly estimate the vibrations and IAS variations generated by the gear mesh. Sun & al. [29] propose a complete model of the profile corrections for the determination of Transmission Error (TE). Since the profile modifications such as profile crowning are usually of small scale compared to the geometry of the teeth, they are assumed in the present work to be assimilable to total deflection reductions depending on the radius of the contact point and not to modify the contact point location nor the orientation of the contact force. A new term $\delta_{corr}\left(r_{jk}\right)$ is then added to the expression of the total deflection as follows:

$$\delta_{jk} = \left(d_{1jk} - d_{2jk} - d_{\theta z,jk}\right) \cdot \vec{n} - D_{jk} - \delta_{corr}\left(r_{jk}\right) \tag{12}$$

Tooth tip fillets are more difficult to implement since their characteristic length is not small compared to the tooth dimensions. The principal modifications due to the introduction of tip relief are the modification of the contact point location on the tooth profile and the modification of the total deflection for a given angular position. The calculation of the total deflection for a contact on the tip fillet is similar to the one of a off-line-of-action contact. The presence of tip fillets leads to a reduction of the angular domain where the separation distance is zero. Fig. 4 compares STE for a classical model (in blue), a model that considers off-line-of-action contact and tip fillets (in red), and a model that considers in addition profile crowning (in black). The geometry of profile modifications implemented here is similar to profile correction performed for real aeronautical gears in use by Safran Helicopter Engines. All modifications lead to a softening of stiffness variations and are then relevant in a dynamic model aiming at estimating the IAS variation due to gears. Simulation shows that profile crowning has a deeper impact on the STE than tip fillets.

2.6. *Damages*

Since the gear model previously described is dedicated to the study of a damaged transmission, spalls and tooth root cracks have been implemented. Fig. 5 shows the geometric parameters implemented for each type of damage. The actual value of these parameters will be discussed in the second part of this paper. The spall is considered as a local decrease of the total deflection. When the location of the contact point is included in the area defining the spall, the total deflection on the corresponding slice is decreased by the depth of the damage. Spalls are supposed to be rectangular and are then determined by five parameters corresponding to their radial location

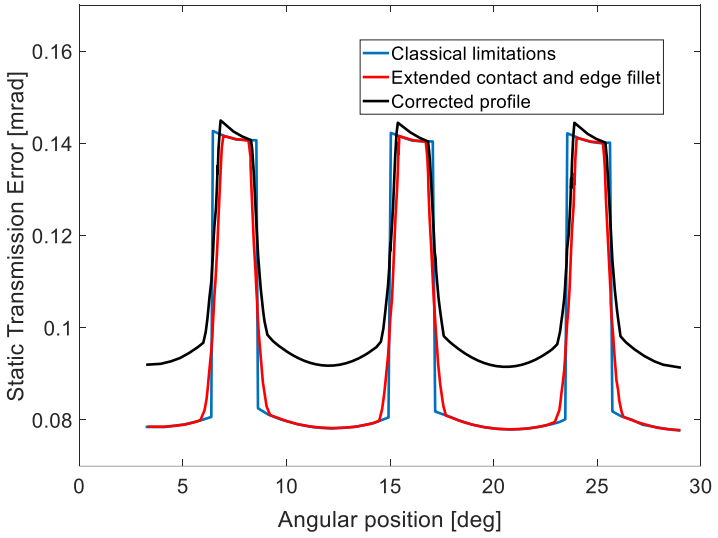

Fig. 4. STE with and without profile modifications.

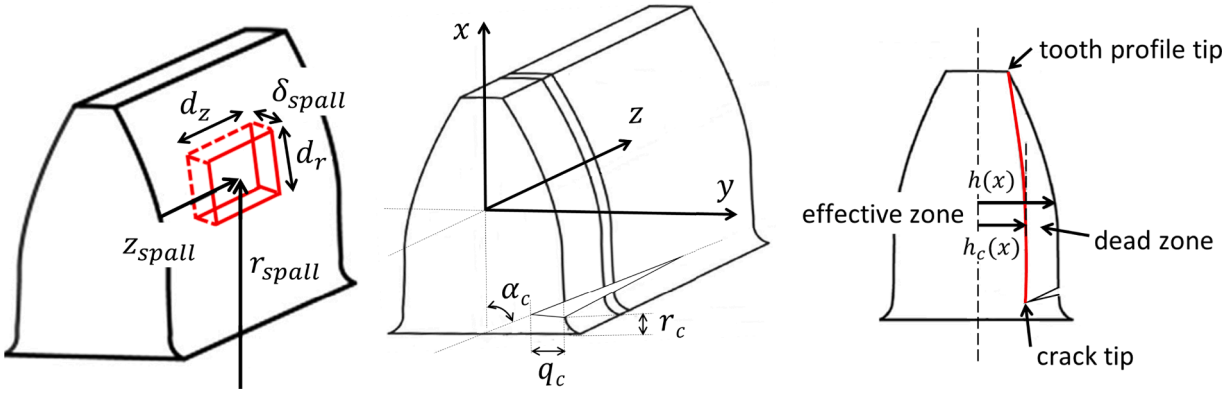

Fig. 5. Implemented damages geometry inspired by [12].

r_{spall}, their radial width d_r, their depth δ_{spall}, their axial location z_{spall} and their axial length d_z. This model is not perfect as some deformation due to an increase of Hertzian deformation on the edges of the spall should be accounted for. The expression of the total deflection in case of contact on a spall is given in Eq. (13):

$$\delta_{jk} = \left(d_{1jk} - d_{2jk} - d_{\theta z,jk}\right) \cdot \vec{n} - D_{jk} - \delta_{corr}\left(r_{jk}\right) - \delta_{spall}\left(r_{jk}, z_k\right) \tag{13}$$

The tooth root crack model is limited to plane cracks. They are defined by a depth law q_c depending on the axial location, an orientation angle α_c and a radial location on the tooth profile r_c as presented in Fig. 5. The stiffness of the cracked tooth is calculated by considering a dead zone as proposed by Chen & al [12] [13],. The width and the area of section of the tooth involved in the determination of stiffness is modified by the presence of crack as follows. The border of the dead zone follows a parabolic law and connects the tooth tip and the crack tip.

$$L(r) = \begin{cases} 2h(r) & if\ r < r_c(z) - q(z)\sin(\alpha_c(z)) \\ h(r) + h_c(r) & else \end{cases} \tag{14}$$

3. Dynamic analysis of an academic transmission

3.1. Simulated system and parameters

The simulation goal is to predict and to understand the dynamic phenomena, their impact on the signal contents and the

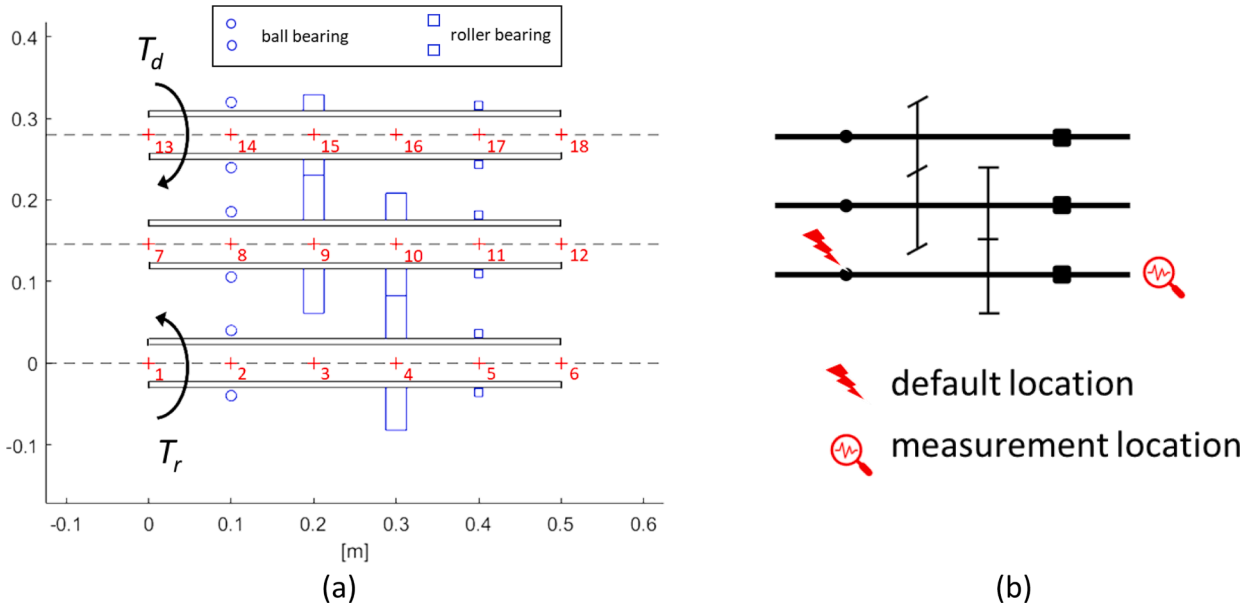

Fig. 6. Simulated system (a) overall overview and (b) its schematic representation.

interactions between the different components of the transmission. The simulated system does not correspond to a real device but the geometries of the different components are realistic and based on actual ones. The transmission is composed of three shafts, two external cylindrical gear stages, three deep groove ball bearings and three cylindrical roller bearings. Fig. 6 schematizes the simulated transmission. All the geometric parameters defining the system and the material properties are summarized in the appendix section.

The three shafts are identical and discretized into five Timoshenko beam elements leading to six nodes per shaft which are numbered from 1 to 18 and marked with red crosses in Fig. 6. Each shaft is maintained by one ball bearing and one cylindrical roller bearing. Since the casing is not modeled, the outer rings of all bearings are built in. The ball bearings are identical to each other as well as the roller bearings. In order to impose different reduction ratio for both gear stages and different working conditions for the bearings, the number of teeth and the helix angle are different for both gear stages. The low-speed gear stage, connecting the low-speed shaft (or output shaft) and the intermediate shaft is a spur gear while the high-speed gear stage has a helix angle of twenty degrees which connects the input shaft and the intermediate shaft. Hence, barely any axial load is transmitted to the low-speed shaft. A driving torque T_d and a resistive torque T_r are applied on the high-speed shaft and the low-speed shaft at nodes 13 and 1 respectively. Furthermore, viscous damping torques are imposed on the nodes corresponding to the bearing inner rings. The damping coefficients are the same for each bearing and are chosen so that the global efficiency of the transmission is set to 90 %, including all the previous losses introduced in gears. The resulting dissipation torque introduced for each bearing is proportional to the shaft rotating speed $T_r = -\alpha_{bea}.\omega$ with

$\alpha_{bea} = 0.015\ N.m.s.rad^{-1}$.

3.2. IAS as a monitoring tool

In the present work, the IAS has been chosen as the monitoring signal because of its advantages. First, the IAS measurement implies a natural angular sampling which is convenient for the monitoring of angular periodic components such as gears or bearings. Second, the IAS carries enough information to the diagnostics the transmission because bearings and gears generate angle-varying torques which lead to IAS variations. When damaged, the signature of these components on the IAS changes in form and in magnitude allowing one to determine the health state of each component by using only the information contained in the IAS signal. In the following, the IAS variation will always be plot as a function of low-speed shaft angular position and not as a function of time. In the same way, in order to highlight gear and bearing behavior, the spectra of the IAS will be plotted using angular frequencies defined as the inverse of the angular length of periods representative of these cyclic behaviors. Angular frequencies are expressed as the number of events per revolution (ev/rev) or as inverse of the angular length in rev^{-1} instead of classical frequencies (Hz or s^{-1}). In this paper, these angular frequencies are defined in reference to the low speed shaft.

IAS is generally used as an additional monitoring signal and measured using an angular encoder coupled with a high frequency clock. It may be then estimated using the “Elapse Time” method by measuring the time between successive pulses on encoder signals. However, this method introduces biases, the most important of which is the quantification bias [30]. An approximation of the theoretical noise generated during measurement is given by André & al. [31]. The level of this noise is higher at high speed because the time separating two pulses of the angular encoder is shorter and the number of clock pulses is smaller which leads to higher quantification error. However, for a system such as the one introduced here, this phenomenon represents no limitation. Fig. 7 exhibits in the angular and frequency domains the real IAS, which is the IAS signal obtained by numerical simulation, and the measured IAS, which corresponds to the IAS signal as it would be observable using sensor on an actual system. This measurement simulation has been performed using a 1000 pulses per revolution angular encoder and a 80 MHz clock. The quantification ceiling has been plotted in black in Fig. 7 and it corresponds to the theoretical limitation of the noise generated by the measurement method. The impact of the measurement on the IAS in angular domain is important and the quantification error can be easily observed. However, its impact on the

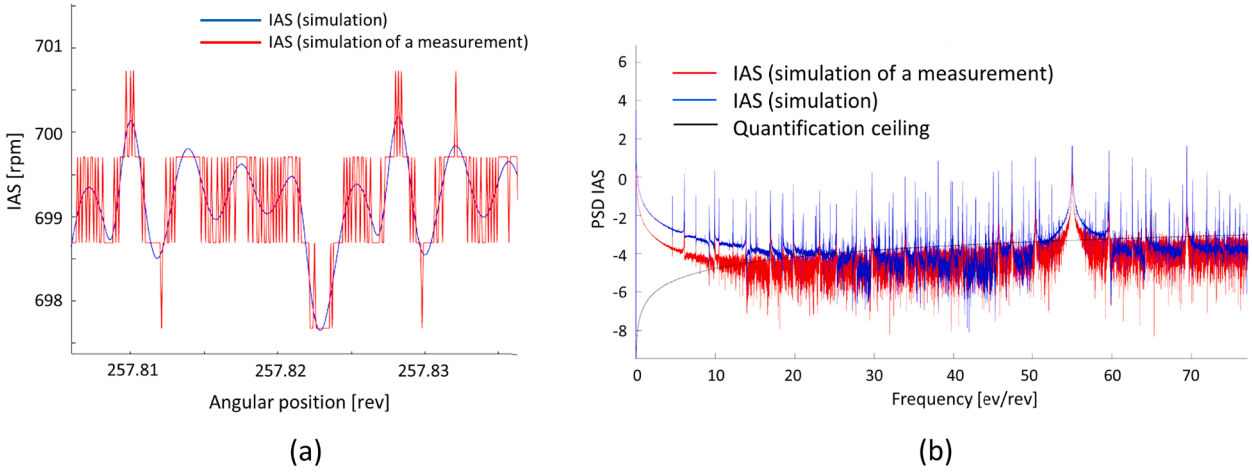

Fig. 7. comparison of IAS and its simulated measurement in (a) angular domain and (b) its Power Spectral Density.

spectrum remains low as the level of noise is clearly lower than that of the spectral components of interest.

All the simulated signals are obtained for a very long duration in the angular domain in order to gain a frequency discretization allowing a clear separation of all the cyclic contents of all the mechanical components.

In the following sections two different operating conditions are used to highlight the benefits of non-stationary condition, IAS measurements as monitoring signal and angular analyses. The load is chosen to reach the operating conditions in speed and the two resulting conditions are described in Table 1.

3.3. Bearing – gear interactions

The dissipative torque generated by rolling resistance inside the bearings depends on the load applied on them. In the simulated system, the only axial and radial loads on the shafts are generated by the gears since the only external forces are the driving and the resistive torques and no unbalance is considered. Consequently, the IAS variations due to bearings can be schematically seen as the product of the mesh forces by a function of the bearing properties and the angular position [19]. Hence, in addition to the characteristic frequencies of the bearings and their harmonics, numerous modulations by these frequencies appear as sidebands around the gear frequencies. As an example, the sidebands spaced at the low-speed shaft ball bearing frequency and its harmonics around the high-speed gear stage frequency are marked in Fig. 8. The contributing mechanical components in the spectra are defined by different symbols and colors depending on the figure, their architecture location being based on the schematic representation in Fig. 6b. These can only be observed with a model that ensures strong coupling between bearing and gear components in non-stationary operating conditions (NSC). Classical gear simulations indeed introduce simplified bearing models such as Palmgren's [24] which does not introduce any angular excitation. Moreover, usual ball bearing dynamic simulations use constant mesh stiffnesses for gears. Even if this kind of focused simulations are useful in order to study the behavior of one component, it does not enable the understanding of their interactions, particularly as modulations.

As shown in Fig. 8, the level of the modulation sidebands is similar to, or even higher than the additive harmonics of the bearing Ball Pass Frequency on Outer ring (BPFO) and its harmonics. Thus, they could be easier to detect and still carry as much information as the BPFO.

The study of these modulations can be complementary to the study of fundamental frequencies in health monitoring. The presence of these sidebands justifies the use of classical demodulation methods but encourages one to focus on the bands around a gear frequency instead of some high frequency resonance when analyzing IAS signals.

3.4. Non-stationary operating conditions and angular approach

The main interest with respect to non-stationary operating conditions is to easily separate the phenomena related to the modal response of the system, which are time-periodic, from the phenomena generated by gears and bearings, the behavior of which is angle-periodic or cyclic. The global system dynamics indeed depends on the rotating velocity and of the interactions between its eigenmodes and the exciting frequencies. Fig. 9 shows an angular spectrogram of the low-speed shaft IAS obtained for an increasing speed. In this figure, the frequencies of several eigenmodes of interest have been plotted in black curves while the horizontal lines correspond to the bearing and gear frequencies. Curves of eigenmodes are curving because the angular spectrogram (or Short Angle Fourier Transform) is performed with a IAS signal sampled in the angle domain. Note that the vertical axis is oriented with increasing orders downward in order to keep the global shape of the speed operating condition.

It is clear that the system dynamic behavior changes depending on the angular position of the shaft and therefore on the angular velocity of shafts. Here again, IAS is another dynamic response of the transmission and is analyzed with classical signal processing tools like FFT. IAS offers another transfer path from excitation to response which is complementary to conventional vibrations.

The magnitude of angle-periodic phenomena increases when their frequencies correspond to those of an eigenmode or a group of eigenmodes. The modulation sidebands spaced at ball bearing frequencies around the gear mesh frequencies appear locally and form "hot" zones in the figure. Health monitoring in steady conditions is hence difficult as it requires a good knowledge of the system behavior at the concerned speed and of the interactions existing between angle and time-periodic phenomena. In the same figure, it can be observed that the resonance phenomena endure after the initial correspondence of cyclic excitations and eigenmodes. Indeed, the energy dissipation through damping is not instantaneous. A simulation in which the angular speed changes rapidly compared to the dynamics of the system leads to results that are more difficult to interpret.

An angular approach and an Angle Fourier Transform decrease the magnitude of time dependent phenomena in the spectrum by spreading out their energy over several angular or cyclic frequencies. Conversely, the angular-periodic parts of the signal, even with small magnitude, are highlighted by the integration effect of the Fourier Transform. Long datasets are then more suitable as they ensure a better mitigation of time related effects. Moreover, the rotating speed variation has to be wide enough to spread out the energy of time related frequencies over wide angular frequency ranges. Finally, the angular range of exposure to each rotational speed has to be as homogenous as possible in order to avoid energy accumulation on one specific angular frequency and the appearance of artifacts

Table 1
speed profiles of stationary and non-stationary conditions.

Almost Stationary Conditions (ASC)	[360 – 430 rpm / 20 rev]
Non-Stationary Conditions (NSC)	[200 – 900 rpm / 300 rev]

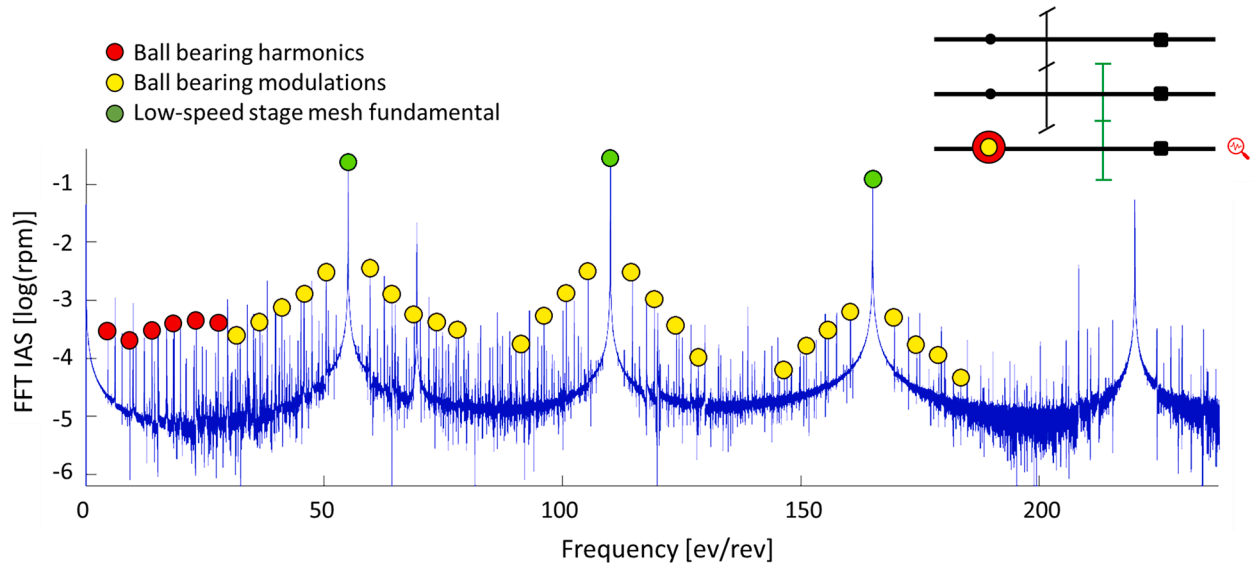

Fig. 8. Modulations by the characteristic frequencies of low-speed shaft ball bearing of the low-speed stage gear mesh frequency.

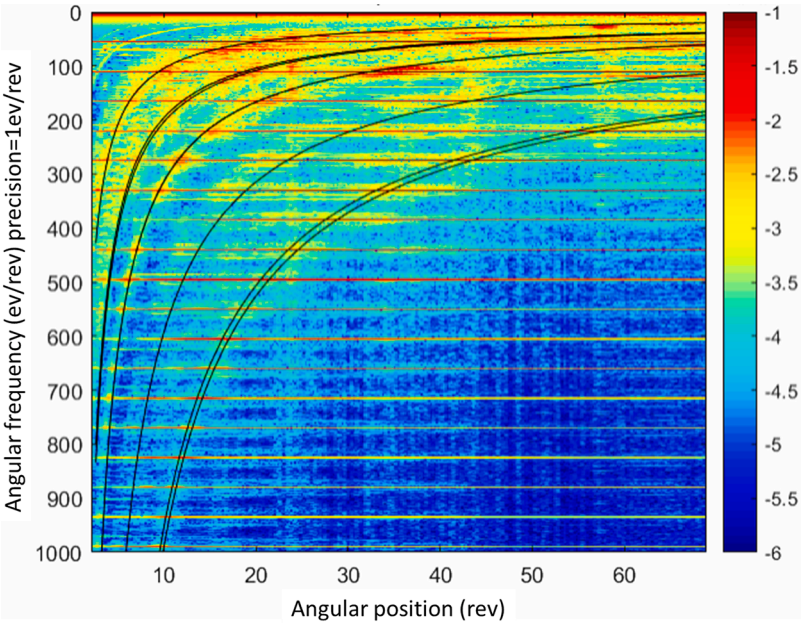

Fig. 9. Low-speed shaft IAS spectrogram for an increasing speed and frequencies of eigenmodes [200 – 900 rpm / 300 rev].

in the spectrum. Fig. 10 and Fig. 11 show the low-frequency portion of the low-speed shaft IAS spectrum obtained for two different simulations of a healthy system. In the first one, the rotating speed ramps up from 360 to 430 rpm during 20 revolutions while in the second one, it moves from 200 to 900 rpm during 300 revolutions. On these figures, the frequencies associated to the low-speed shaft ball bearing and the high-speed gear stage are highlighted with color markers. For clarity reasons, only the first harmonics and the first modulation sidebands are marked.

For the first simulation, the angular spectrum clearly contains time-dependent artifacts due to the small range of angular speed used. Two kinds of behavior are visible in Fig. 10 and are delimited by black dotted lines. The first one is associated to isolated eigenmodes and leads to enlarged peaks in the spectrum. An example can be observed in the range [16-19] events per revolution. The width of the peak corresponds approximately to 20 % of its frequency which is explained by the variation of 20 % of the rotational speed. This peak has no rectangular shape because the rotational speed variation is not linear in angle in this simulation but has a parabolic shape and the exposure to different speeds is then not homogenous. The second kind of behavior occurs when several

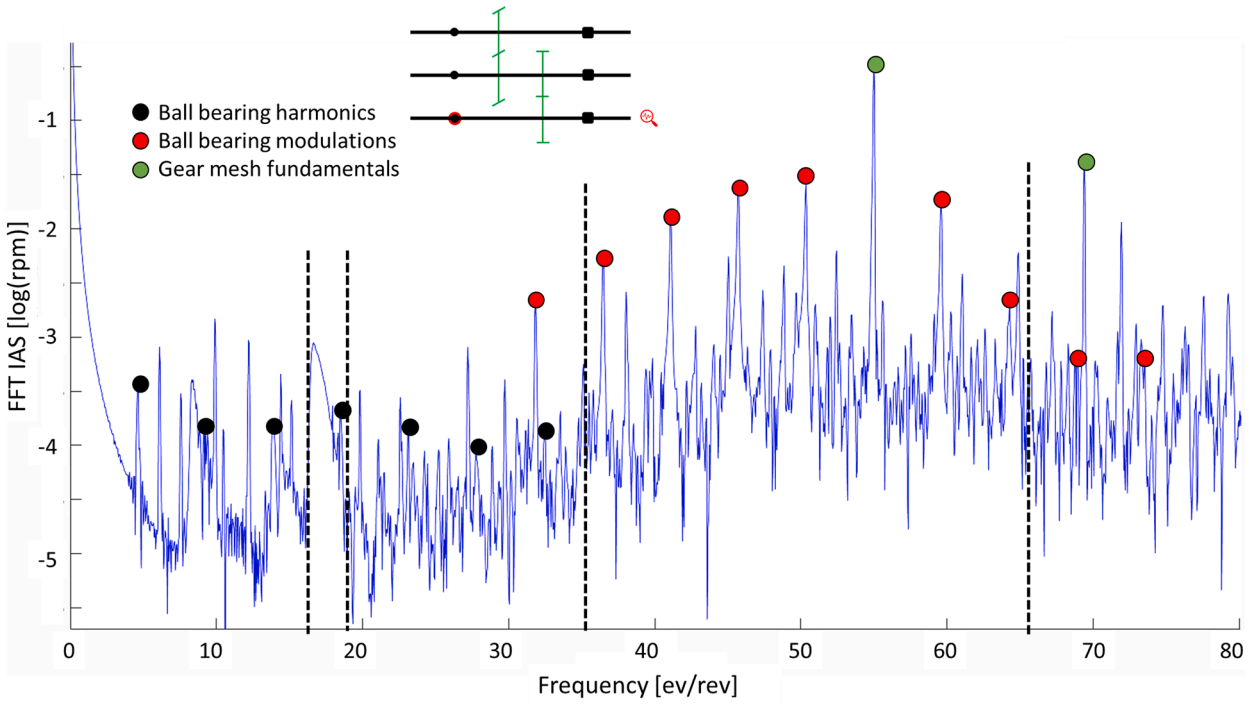

Fig. 10. Angular spectrum of low-speed shaft IAS for a quick and low increase of rotating speed [800–1000 rpm / 20 rev].

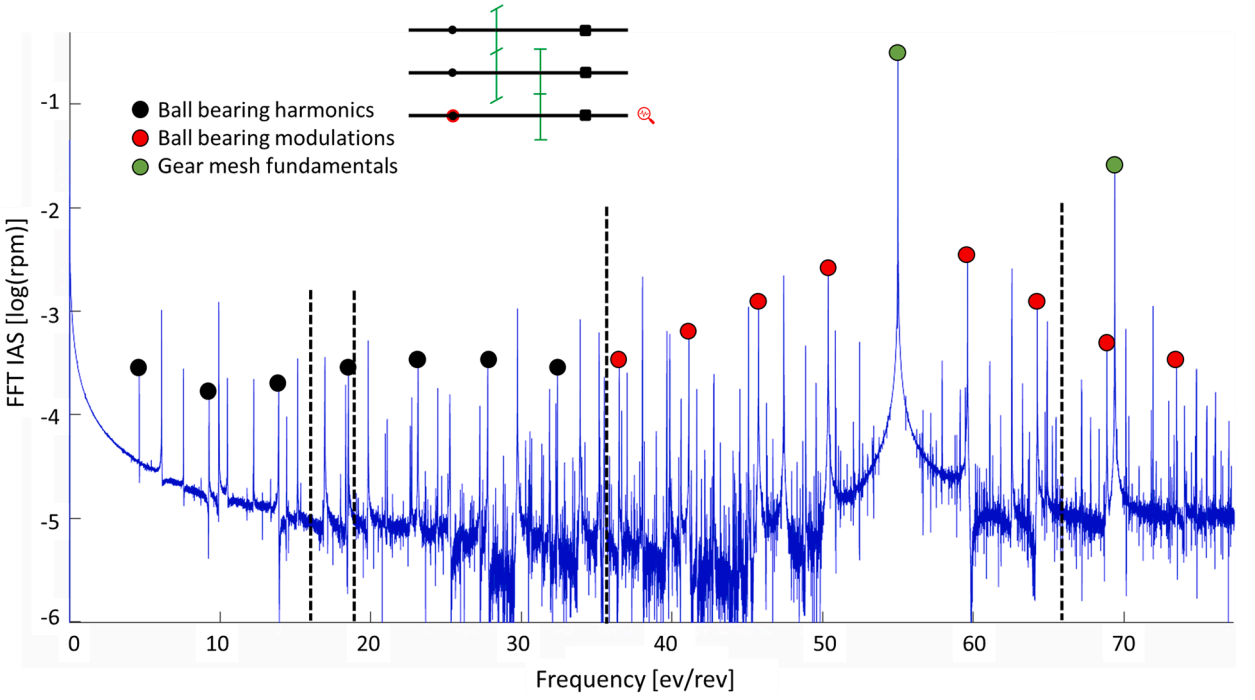

Fig. 11. Angular spectrum of low-speed shaft IAS for a slow and long increase of rotating speed [200 – 900 rpm / 300 rev].

eigenmodes have similar frequencies and create a wide range of frequencies in which the system response is magnified. This can be observed in the range [35–65] events per revolution. It accentuates the modulation sidebands spaced at ball bearing frequencies around the high-speed gear stage frequency in this zone while these modulations are difficult to detect outside of it. For this simulation, the characteristic frequency of low-speed shaft ball bearing and its harmonics are difficult to detect and partially hidden in the base noise level of the spectrum.

For the second simulation with longer dataset and wider range of angular speed variation including the previous range of speed variation, the time related components are eliminated from the spectrum. The same dotted lines as in the previous figure have been drawn and it can be observed that the phenomena described in Fig. 10 such as the 16–19 events per revolution resonance or the spectrum foot shape are not visible in Fig. 11. This leads to balanced modulations spaced at the BPFO of low-speed shaft ball bearing around the gear mesh fundamental since they are no longer affected by time related phenomena during the whole simulation. This should obviously facilitate the implementation of demodulation methods in angular domain analysis. Consequently, long simulations under non-stationary conditions are best suited to gear and bearing monitoring since they allow the focus on their behavior by removing the effect of the structure dynamic response. In this way they can be seen as a simple alternative to complex and expensive deconvolution methods. Furthermore, longer datasets allow higher frequency precision and a better separation of the various phenomena in the spectrum. However, they require higher computation time for simulation but they do not suffer from irregular sampling in the angular domain.

During real experiments, it could be profitable to voluntarily impose stationary working conditions and choose the rotating speed so that one or several eigenmodes magnify some chosen frequencies in order to make the detection easier. Nevertheless, this requires a deep knowledge of the system behavior under faulty and healthy conditions at the selected speed in order to ensure a correct processing of the collected data. Processing data under non-stationary conditions offers the possibility to avoid such signal perturbations and requires only the knowledge of the transmission kinematics.

3.5. Health monitoring of a power transmission

3.5.1. Detection of distant components

One of the main benefits of the use of IAS as a monitoring tool is the possibility to monitor a whole transmission using one single sensor. A component generating a perturbing torque on one shaft indeed also affects the IAS of the other shafts through gear transmissions even in healthy condition [1,19,21,22]. As shown in Fig. 12 it is possible to detect the signature of the second gear stage on the low-speed shaft. On the same spectrum, the signature of the ball and roller bearings of the high-speed shaft are also visible. They appear as harmonics of the BPFOs and as a modulation by them of the gear mesh frequencies. The presence of damage on one of these distant components would be detectable through an increase of its signature in the spectrum. The detection is possible in both ways. The signature of ball and roller bearings of the low-speed shaft being also visible on the high-speed shaft IAS.

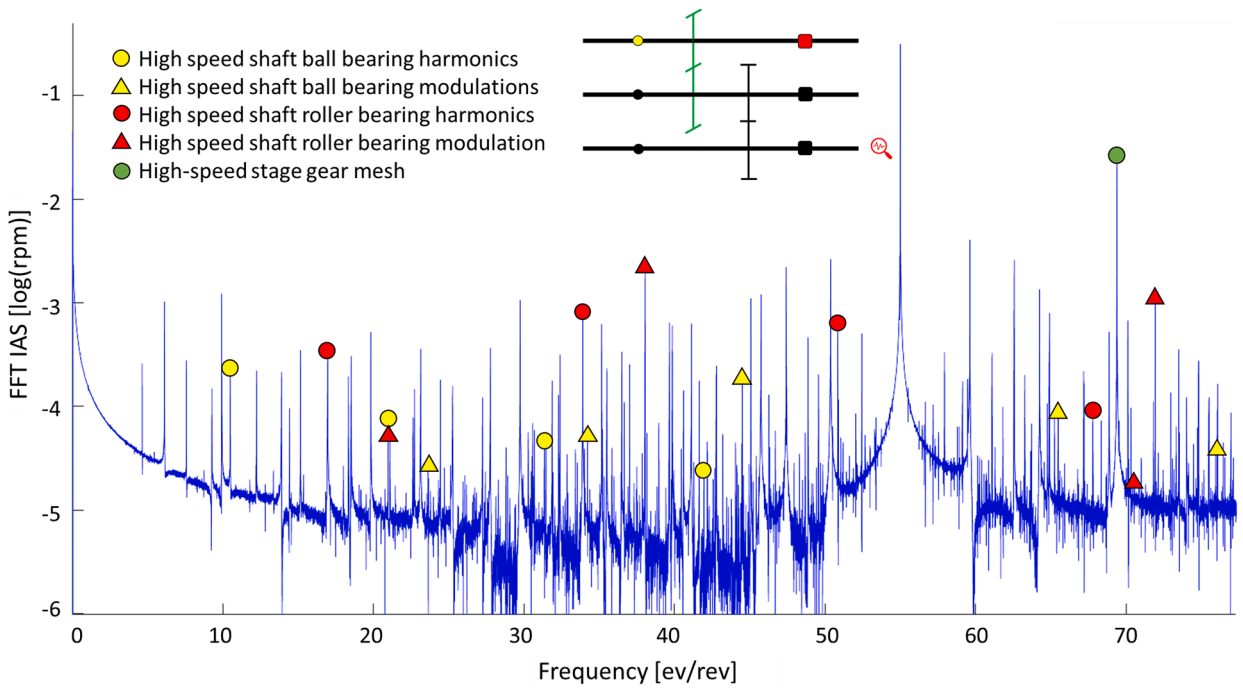

Fig. 12. Signatures of high-speed shaft components on the low-speed shaft [200 – 900 rpm / 300 rev].

3.5.2. Bearing damage

When it comes to bearings, the damages often take the form of a spall. The distribution of the load over the rolling elements is affected each time one of them passes over the spalled area. This modifies the resistive torque due to rolling resistance in the bearing and then creates a small perturbation of the IAS through torque fluctuations. In order to study the impact of this kind of damage on the global dynamic of the system, a spall is implemented on the outer race of the ball bearing of the low-speed shaft. The spalled area is located in the direction of the radial load since it is the place where the contacting forces and the contact pressures are the highest ones and then the place where real damage are most likely to appear. The spall consists of a removal of material of 100 μm in depth, which is similar to typical real spall depth, as shown in Fig. 13. Its length corresponds to the third of the angular space separating to consecutive balls and it covers one quarter of the race in width. Hence, the implemented spall is a just propagated one since the objective is to show that this kind of damages are detectable using IAS even briefly after it initiates.

Fig. 14 compares the spectra obtained for healthy and damaged bearings. The BPFO and its harmonics have been marked with dots and their sidebands from modulation of the gear mesh have been marked with squares. The number of harmonics and their magnitude increase in the presence of a fault which makes it easily detectable. However, the magnitude of the sidebands spaced at the bearing frequencies around the high-speed gear stage frequency, marked with squares, decrease.

From these first and initial results some indicators should be proposed as, for instance, the difference between increases in the magnitude of harmonics and decrease in the magnitude of modulation sidebands. It is beyond the scope of this study to investigate the robustness of these indicators, especially if one takes advantage of the non-stationary conditions that were not used in this preliminary example.

3.5.3. Gear mesh damage

As mentioned previously, the implemented gear damages can either be tooth root cracks or spalls. The first kind of damages leads to a decrease of the affected tooth stiffness while the second one leads to a decrease of the total deflection of the tooth. In both cases, the damage generates a perturbation of IAS when the damaged tooth is under load. The characteristic frequency of both damages is then the same since such a perturbation appends once per revolution. One simulation has been carried out for each kind of damage. They have both been implemented on the low-speed shaft wheel, the angle helix of which is zero. The implemented crack is uniform along the tooth width and its depth, its location and its orientation do not vary with the axial position on the tooth flank. This choice is justified by the absence of phenomenon leading to the wear of one particular side of the teeth rather than the other in the modeled system. The crack depth is equal to roughly 15 % of the tooth thickness which corresponds to a substantial damage (normal crack condition). It is located at the tooth root where the stresses are known to be the most important.

Coming to the gear spall description, the spall covers half of the width of the tooth and is located at its center in the axial direction. It is centered on the pitch radius and cover one third of the tooth height. This has been chosen since this area correspond to the position of contact point where only one tooth pair are in contact and when the contact forces are the highest. The depth of the spall is fixed at 100 μm which corresponds to real spall typical depth. Fig. 15 presents the geometries of the implemented damages.

Fig. 16 compares the IAS spectra of low-speed shaft obtained for healthy and cracked gears. For the damaged one, a perturbation at one event per revolution appears as well as harmonics at every order up to 40 events per revolution. The corresponding frequencies have been marked with red dots in the figure. It is then easy to detect the presence of damage on the gear by using the IAS spectra. The other components of the spectrum remain perfectly unchanged. The presence of fault on the low-speed shaft wheel seems then not to interfere with the behavior of the bearing or the low-speed gear stage.

A second simulation has been performed with a deeper crack propagating on 25 % of the tooth thickness (deep crack condition).

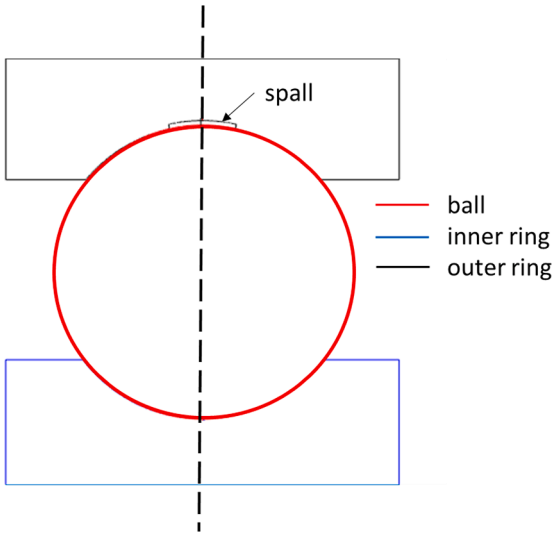

Fig. 13. Spall geometry.

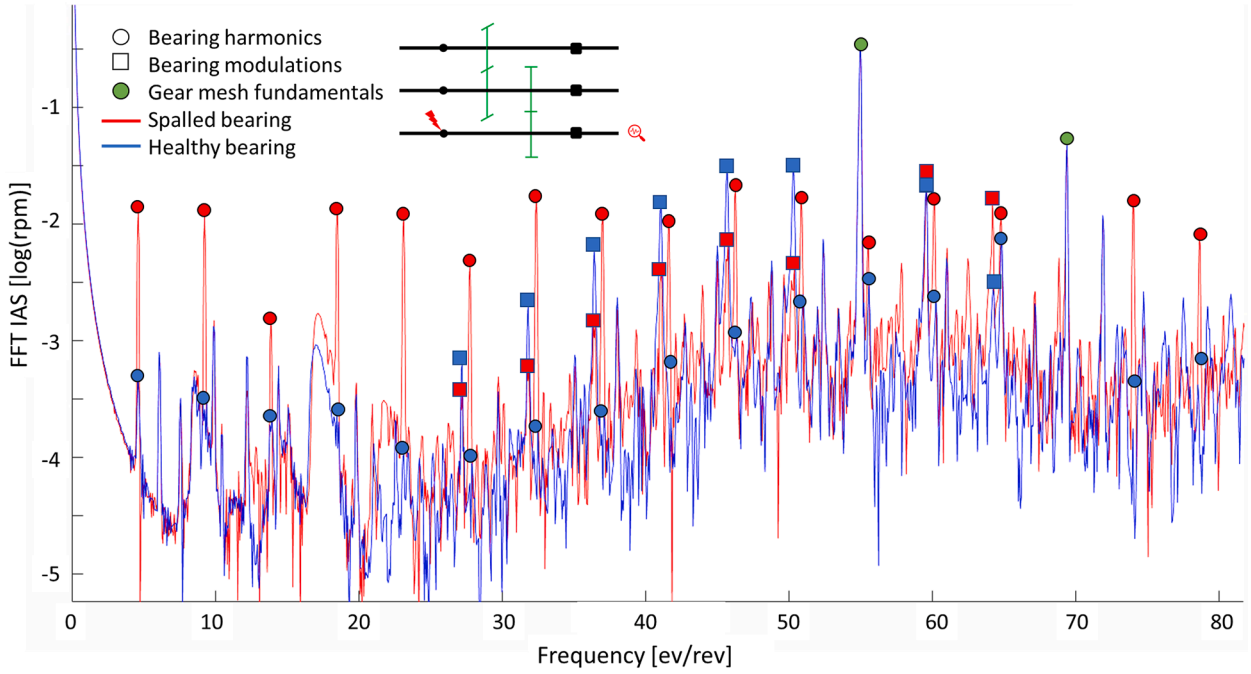

Fig. 14. Comparison of low-speed shaft IAS spectra for a healthy (blue) and a damaged (red) ball bearing [360 – 430 rpm / 20 rev]. (For interpretation of the references to colour in this figure legend, the reader is referred to the web version of this article.)

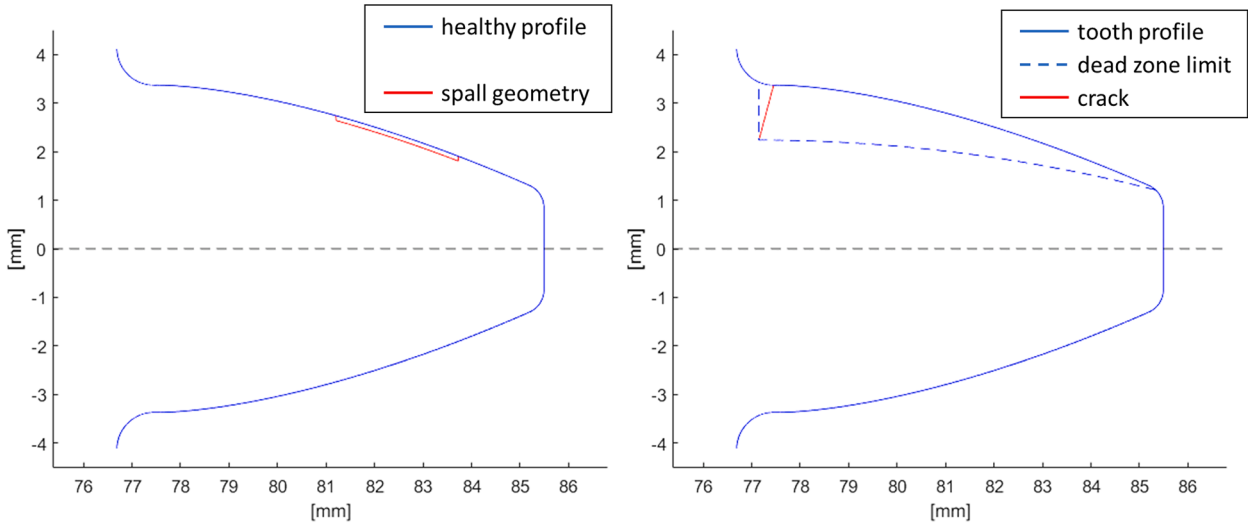

Fig. 15. Geometry of implemented damages.

This has proven that the gravity of the damage plays a role in the IAS perturbation. Fig. 17 shows that the magnitude of the frequency components at integer orders increase with the depth of the crack. Considering the spall damage, the observations are the same with a noticeable increase of integer shaft order frequencies and they are not detailed in a dedicated figure. Hence, it is possible to detect the presence of damage and to estimate its gravity by monitoring the presence and the magnitude of frequency components at integer orders.

Fig. 18 compares IAS spectra for spalled and cracked gears. In both cases, the peaks associated to the damage are marked with dots. The IAS perturbation introduced in both cases is very similar which makes it difficult to distinguish the type of damage when it comes to health monitoring. The only observable difference on the spectrum is that the peaks associated to the crack sink a bit faster into the base noise level of the spectrum for the highest harmonics. This is to be expected since the duration of the effect of the crack is of the same order as the tooth mesh period, whereas it is shorter for the (modelled) spall as it can be seen in Fig. 20.

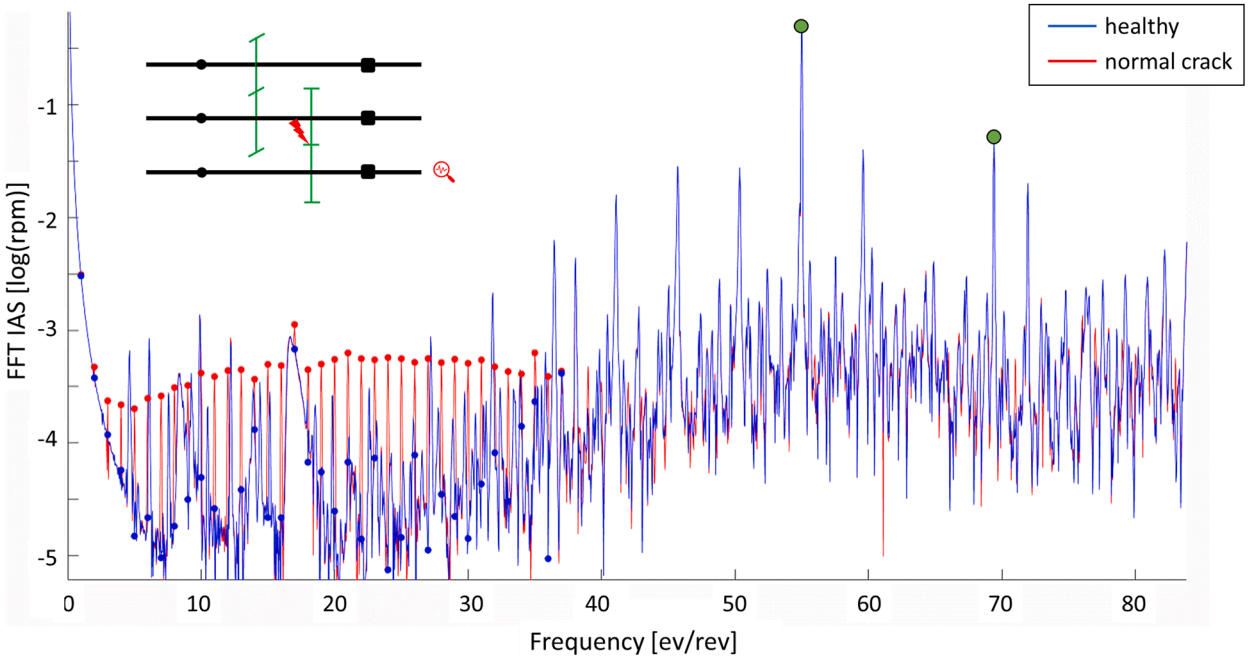

Fig. 16. Low-speed shaft IAS spectra for healthy and cracked gears [360 – 430 rpm / 20 rev].

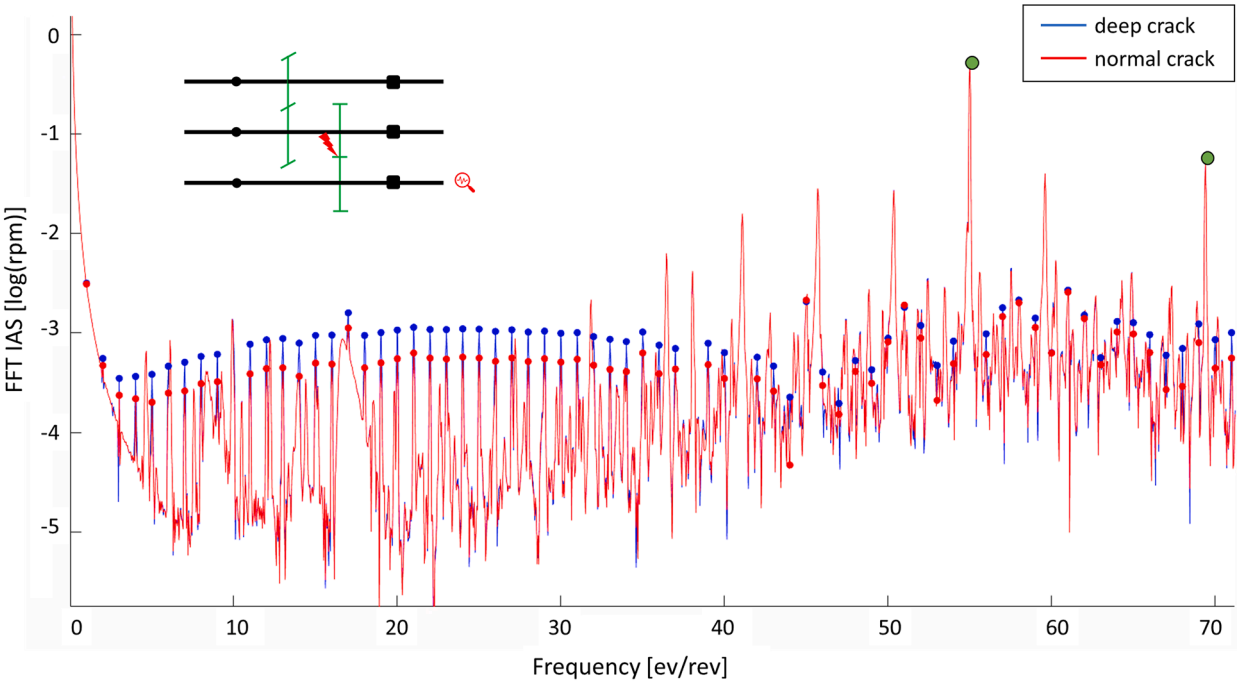

Fig. 17. Low-speed shaft IAS spectra for two crack depths [360 – 430 rpm / 20 rev].

In order to build a more efficient indicator that better separates the two origins of gear failure, it is possible to use signal processing tools such as cepstrum, estimated from the angular spectrum.

In Fig. 19, it is clearly proved that the spalled gear introduces a one revolution periodic phenomenon with higher energy in IAS signal. In the first graph, healthy condition and normal cracked gears are compared in order to highlight the emergence of these one-revolution rahmonics. In the second graph, the comparison of spalled and deep cracked conditions clearly shows that the spall default is proved to be more energetic on these rahmonics.

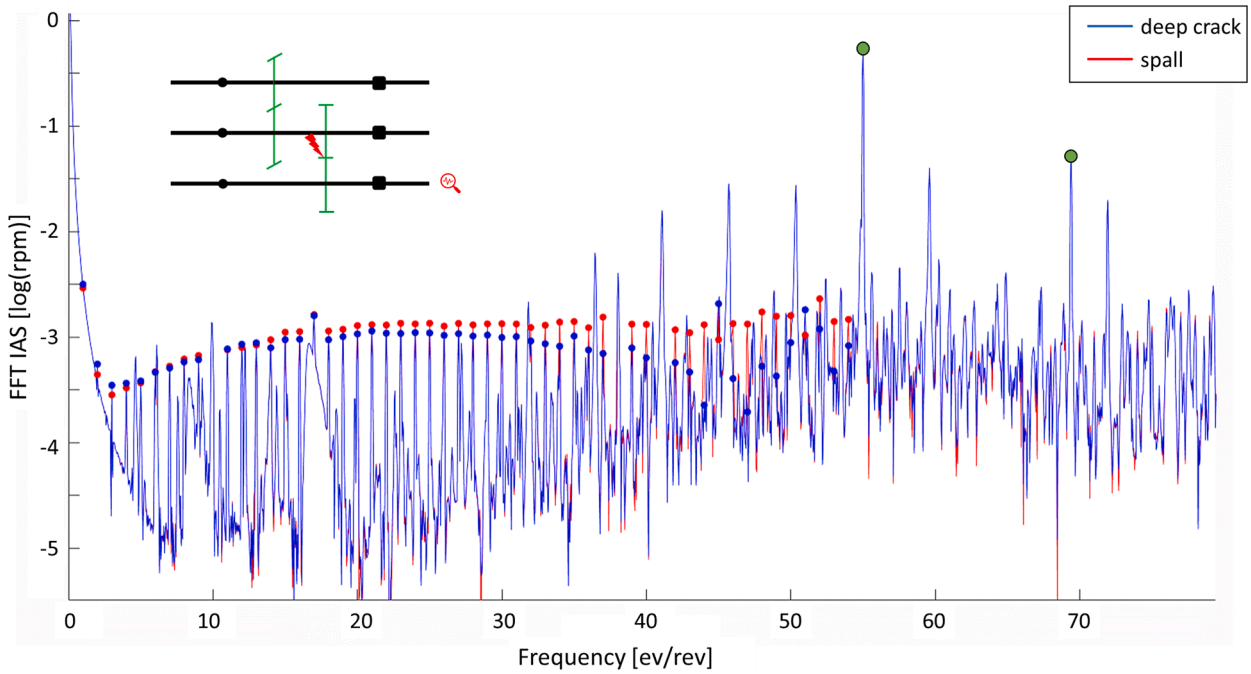

Fig. 18. Low-speed shaft IAS spectra for spalled and cracked gears [360 – 430 rpm / 20 rev].

In order to check this fact Fig. 20 shows the low-speed shaft IAS difference between a healthy gear and a cracked one (red curve) and the IAS difference between a healthy and a spalled gear (blue curve) over more than one revolution of the low-speed shaft. The magnitude of these differences is small but, once per revolution, a disruption appears that correspond to the establishment of the contact on the damaged tooth and, a bit later, to the loss of contact on the previous tooth pair. As well as for a crack, an important difference exists at every entry in contact of the spalled tooth. However, the second impulse linked to the loss of contact on the previous tooth pair has a higher magnitude for a spall damage.

In a real system, phenomena such as unbalance can lead to excitation at the same frequencies as tooth damages and make the diagnosis even harder.

4. Conclusion

This paper proposes a model of a power transmission suitable for the study of the dynamic behavior of gears and bearings. The main goals are to correctly describe and analyze the interactions existing between these two kinds of components and to characterize the influence of a damage on the global dynamics of the system including modal (structural) behavior. For these purposes, a classical model of shafts using Timoshenko beam elements is implemented. Particular attention was paid to the modeling of the gears and bearings as connecting forces, allowing strong couplings between these elements through torque perturbations. The bearing model has been detailed in a previous paper and links the contact forces to the resistive torque in order to introduce a realistic IAS perturbation. It also considers damages like spalls. The gear model is based on the discretization in thin slices of the teeth and a classical stiffness estimation with a precise estimation of connecting forces between the two wheels. The rigid body motions in rotation are kept for all shaft rotation and no particular assumption on speed is made as rotating speeds are considered as outputs of the model. It is refined by taking account for tip relief, profile corrections and off-line-of-action contacts. Finally, two kinds of gear damage are implemented: a spall and a tooth root crack.

Several simulations have been carried out. The comparison of the results obtained for different operating conditions has highlighted the superiority of non-stationary regimes and angular approach when it comes to bearing and gear monitoring. The capability of IAS to monitor the whole transmission using one single sensor has also been theoretically demonstrated, showing the relevance of this tool for rotating machinery monitoring. The simulations integrate the modeling of the measurement principle to better demonstrate the sensitivity of IAS. The use of non-stationary conditions and angular approaches have been proven to be relevant for the monitoring of bearings and gears. They can be seen as substitute for classical signal processing methods such as the deconvolution.

Comparisons between the results of healthy and damaged systems showed that the detection of failure isn't too difficult when monitoring the right frequencies and the evolution of the magnitude in the IAS spectrum. However, the precise diagnosis of gears is arduous since every tooth damage will induce a cyclic excitation located at once per revolution and could be masked by other phenomena such as unbalance. One solution could be the use of the IAS of a distant shaft on which the signature of the gear would not correspond to an integer order. The use of signal processing tools such as Cepstrum could also be profitable and would require the

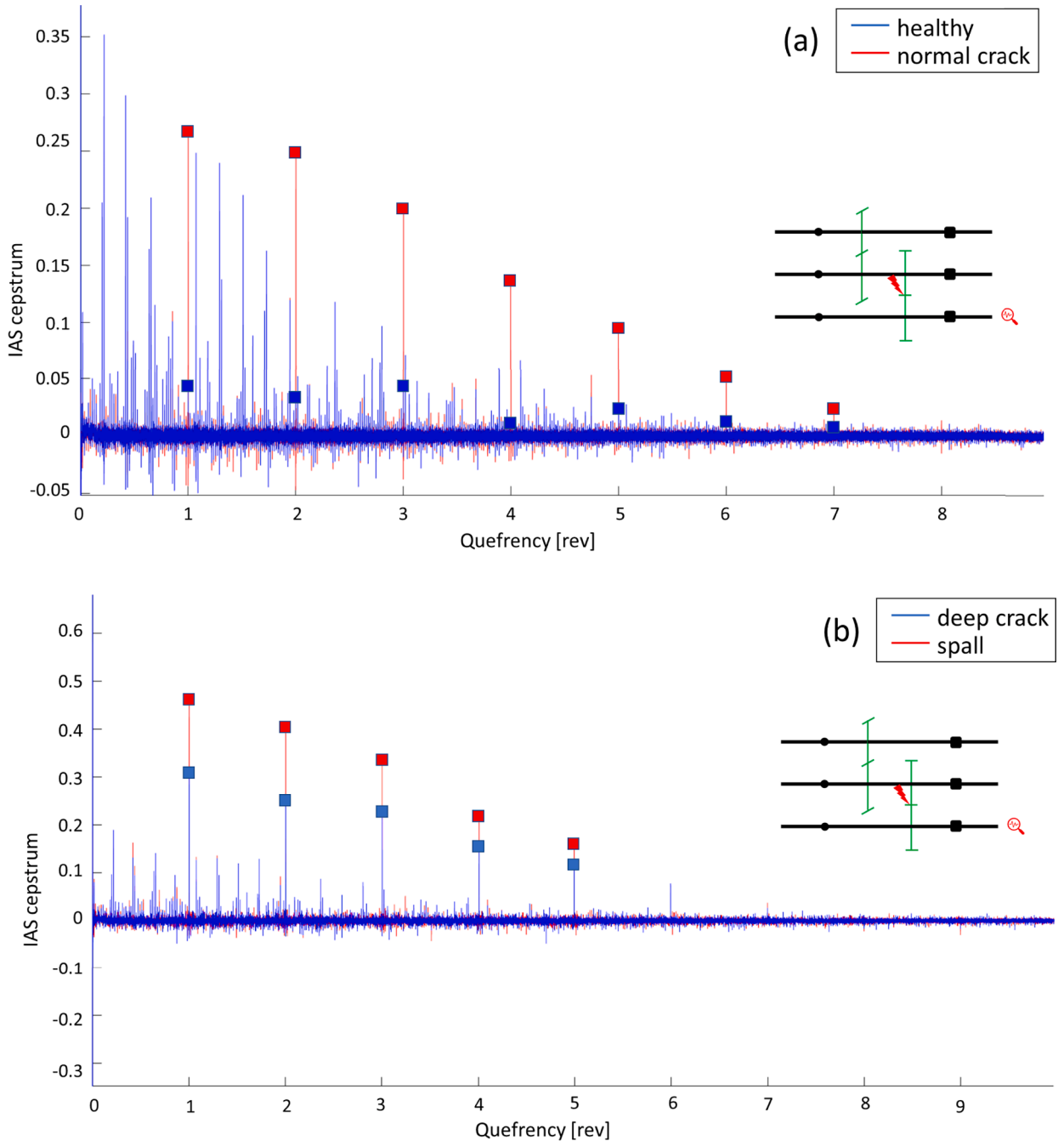

Fig. 19. Low-speed shaft IAS cepstrum for (a) healthy and normal cracked gears, and (b) spalled and deep cracked gears [360 – 430 rpm / 20 rev].

mastery of these tools and angular approaches.

The spectra introduced in this paper are complex but do not include all the characteristic frequencies of real systems. For instance, the only forces applied on the bearings have a fixed direction so that only the BPFO appears in the IAS spectrum. In the presence of rotating forces or inner race damages, their BPFI would also be visible. Moreover, the model proposed here is limited to shafts, bearings and gears. One extension of this work could be the introduction of the wheel flexibility and of the casing [32]. In the same way, a more precise model of the power source (electrical motor) and the load would generate new spectral components in the angular spectrum [33].

One logical and natural extension of this work would be the establishment of numerical indicators allowing a fast and easy diagnosis of a rotating assembly. All these models and simulations are claimed to be realistic signal generators for the investigation of signal processing methods and for the validation of behavior monitoring indicators, exploring non-stationary operating conditions. It

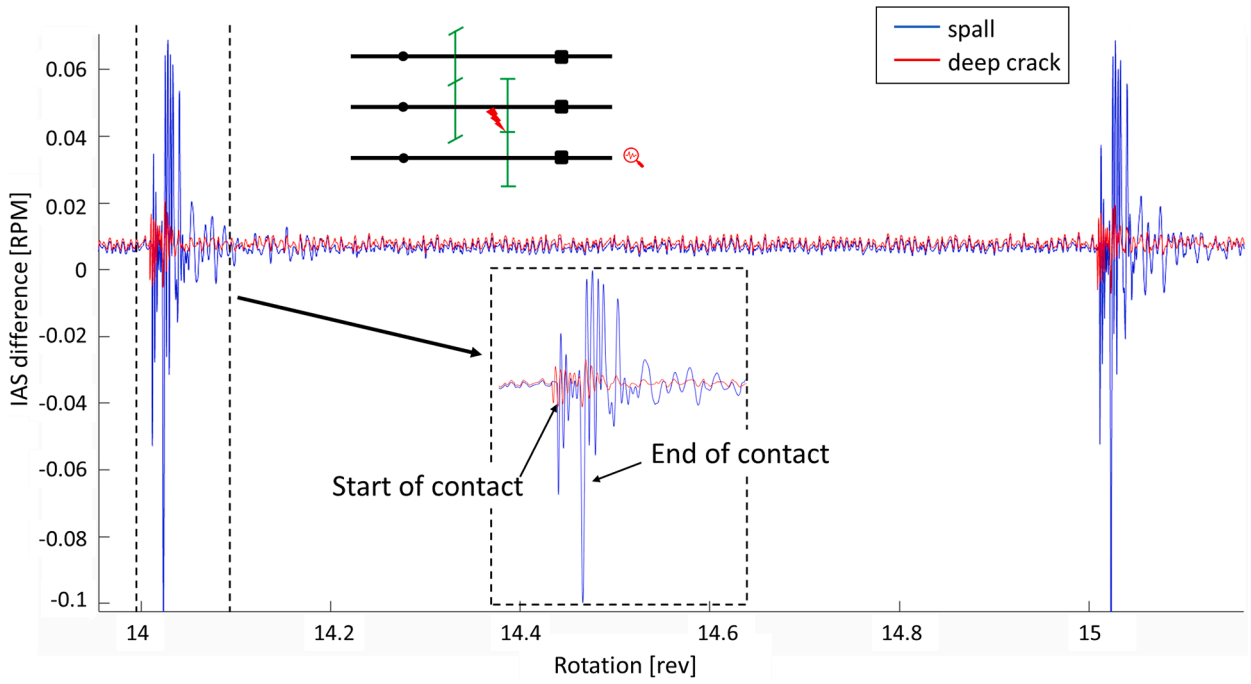

Fig. 20. Low-speed shaft IAS difference between healthy and cracked gears [360 – 430 rpm / 20 rev].

could also be profitable to compare the numerical result obtained through simulation to experimental ones in order to validate the assumptions made in the model and to analyze the influence of external sources of noise on the frequencies of interest.

CRediT authorship contribution statement

Nathanael THIBAULT: Writing – review & editing, Visualization, Validation, Software, Resources, Methodology, Investigation, Formal analysis, Data curation. **Adeline BOURDON:** Writing – review & editing, Supervision, Software, Methodology, Investigation, Formal analysis, Data curation. **Didier RÉMOND:** Writing – review & editing, Writing – original draft, Supervision, Project administration, Investigation, Funding acquisition, Formal analysis, Conceptualization. **Damien LECOUVREUR:** Supervision, Resources, Project administration, Funding acquisition, Conceptualization.

Declaration of competing interest

The authors declare the following financial interests/personal relationships which may be considered as potential competing interests:

Nathanael THIBAULT reports financial support was provided by Association Nationale de la Recherche et de la Technologie. If there are other authors, they declare that they have no known competing financial interests or personal relationships that could have appeared to influence the work reported in this paper.

Data availability

The data that has been used is confidential.

Acknowledgements

This work was supported by the French National Agency of Research and Technology (ANRT), CIFRE [grant number 2019/1353] and Company SAFRAN Helicopter Engines. The work is also involved in the framework of the CIRTrans. All of them are gratefully acknowledged for their support.

Appendix 1. Nomenclature

M	General mass matrix of the dynamical system
C	General damping matrix of the dynamical system
K	General stiffness matrix of the dynamical system
X	State vector containing all the degrees of freedom
F_{ext}	External load vector
F_g	Restoring force vector in the gear stages
F_b	Restoring force vector in the bearings
$(x_i, y_i, z_i, \theta_{xi}, \theta_{yi}, \theta_{zi})$	Translational and rotational positions of the center of the wheel i
E	Young modulus
G	Shear modulus
ν	Poisson coefficient
I	Moment of inertia of tooth
A	Area of section of tooth
$L^*,\ M^*,\ P^*,\ Q^*$	Coefficients from polynomial regressions for fillet-foundation calculation
K_f	Fillet-foundation stiffness
K_b	Tooth bending stiffness
K_f	Tooth shear stiffness
K_f	Tooth contact stiffness
K_{tot}	Total tooth stiffness
δ_c	Tooth contact deflection
F_{jk}	Load applied on slice k of tooth j
δ_{jk}	Total tooth deflection of slice k of tooth j
$\overrightarrow{v_t}$	Tangential component of the relative speed of the bodies
$\overrightarrow{v_1},\ \overrightarrow{v_2}$	Speed of body 1 or 2
$\overrightarrow{n},\ \overrightarrow{t}$	Normal and tangential direction
$\overrightarrow{d_{1jk}},\ \overrightarrow{d_{2jk}},\ \overrightarrow{d_{\theta_z 1jk}}$	Displacement in translation and rotation of wheel 1 and 2
D_{jk}	Separation distance
δ_{corr}	Tip fillet or tooth profile corrections
δ_{spall}	Spall depth
$z_{spall},\ r_{spall},\ d_z,\ d_r$	Geometric spall parameters: location on tooth profile, width and height
$\alpha_c,\ q_c,\ r_c$	Geometric crack parameters: orientation angle, depth law, radial location

Tables 1-4

Appendix 2. Model parameters

This appendix gathers all the material and geometric parameter used in the transmission model given in the second part of the paper.

Table 1
Shaft material and geometric parameters.

Parameter	Value
Shaft length	500 mm
Internal diameter	45 mm
External diameter	60 mm
Young's modulus	210 GPa
Poisson's coefficient	0.3
Density	7800 kg/m^3

Table 2
Gear material and geometric parameters Gears are without profile modification, center distance correction or other gear optimization.

Parameter	low speed gear stage	high speed gear stage
Number of teeth	55/42	53/31
Helix angle	0°	20°
Addendum radius	85.5 / 66 mm	87.6 / 52.5 mm
Dedendum radius	76.8 / 58.5 mm	80 / 45 mm
Teeth width	25 mm	
Normal pressure angle	20°	
Normal modulus	3 mm	
Tip fillet radius	0.5 mm	
Young's modulus	202 GPa	
Poisson's coefficient	0.255	

(*continued on next page*)

Table 2 (*continued*)

Parameter	low speed gear stage	high speed gear stage
Density	7850 kg/m^3	
Artificial friction coefficient	0.03	
Squeeze-film damping	100 N.s.m^{-1}	

Table 3
Ball bearing material and geometric parameters.

Parameter	Value
Number of balls	11
Pitch diameter	80 mm
Ball diameter	12.7 mm
Relative curvature IR	0.51
Relative curvature OR	0.5175
Total radial clearance	45 μm
Young's modulus	179 GPa
Poisson's coefficient	0.3
Density	7870 kg/m3
Torque dissipation coefficient	0.015 N.m.s.rad^{-1}

Table 4
Roller bearing material and geometric parameters.

Parameter	Value
Number of rollers	18
Pitch diameter	72.5 mm
Roller diameter	10 mm
total roller length	10 mm
Roller curvature radius	350 mm
Roller fillet radius	1.1 mm
Total radial clearance	40 μm
Total axial clearance	20 μm
Shouldering presence	BE only
Young's modulus	179 GPa
Poisson's coefficient	0.3
Density	7870 kg/m^3
Torque dissipation coefficient	0.015 N.m.s.rad^{-1}

Appendix 3. Fillet foundation stiffness

The fillet foundation stiffness is estimated with an analytical expression from Sainsot et al. [11] and coefficients L^*, M^*, P^*, Q^* are obtained using polynomial regression based on FE results.

$$\frac{1}{K_f} = \frac{\cos^2(b_{eff})}{E\delta z}\left[L^*\left(\frac{d}{S_{root}}\right)^2 + M^*\frac{d}{S_{root}} + P^*\left(1+Q^*\tan^2(b_{eff})\right)\right] \tag{3.1}$$

The expression of each coefficient X^* is based on a common polynomial expression (3.2):

$$X^* = \frac{A_X}{\theta_f^2} + B_X\left(\frac{R_f}{R_a}\right)^2 + C_X\frac{R_f}{\theta_f R_a} + \frac{D_X}{\theta_f} + E_X\frac{R_f}{R_a} + F_X \quad X^* \in \{L^*; M^*; P^*; Q^*\} \tag{3.2}$$

Where the coefficients A_X, B_X, C_X, D_X, E_X and F_X are given in the following Table 5.

Table 5
Calculation coefficients for polynomial expression L^*, M^*, P^*, Q^* [11].

	A_X	B_X	C_X	D_X	E_X	F_X
L^*	$-5.574\ 10^{-5}$	$-1.9986\ 10^{-3}$	$-2.3015\ 10^{-4}$	$4.7702\ 10^{-3}$	0.0271	6.8045
M^*	$60.111\ 10^{-5}$	$28.100\ 10^{-3}$	$-83.431\ 10^{-4}$	$-9.9256\ 10^{-3}$	0.1624	0.9086
P^*	$-50.952\ 10^{-5}$	$185.50\ 10^{-3}$	$0.0538\ 10^{-4}$	$53.3\ 10^{-3}$	0.2895	0.9236
Q^*	$-6.2042\ 10^{-5}$	$9.0889\ 10^{-3}$	$-4.0964\ 10^{-4}$	$7.8297\ 10^{-3}$	−0.1472	0.6904

References

[1] H. André, A. Bourdon, et D. Remond, «On the use of the Instantaneous Angular Speed measurement in non-stationary mechanism monitoring», in: *Proceedings of the ASME 2011 International Design Engineering Technical Conferences and Computers and Information in Engineering Conference. Volume 1: 23rd Biennial Conference on Mechanical Vibration and Noise, Parts A and B*. Washington, DC, USA. August 28–31, 2011, pp. 15–24, https://doi.org/10.1115/DETC2011-47470.
[2] D. Rémond et, J. Mahfoudh, «From transmission error measurements to angular sampling in rotating machines with discrete geometry», Shock Vib. 12 (2) (2005) 149-161.
[3] J. Wang, «Numerical and Experimental Analysis of Spur Gears in Mesh», Curtain University of Technology, 2003.
[4] J. Brauer, «A general finite element model of involute gears», Finite Element. Anal. Des. 40 (2004) 1857-1872.
[5] A.F. Del Rincon, F. Viadero, M. Iglesias, P. García, A. De-Juan, R. Sancibrian, «A model for the study of meshing stiffness in spur gear transmissions», Mech. Mach. Theory. 61 (2013) 30-58.
[6] J. Teixeira Alves, «Définition Analytique Des Surfaces De Denture Et Comportement Sous Charge Des Engrenages Spiro-Coniques», INSA Lyon, 2012.
[7] C. Weber, The Deflection of Loaded Gears and the Effects On Their Load Carrying Capacity, Department of Scientific and Industrial Research, 1949.
[8] C. Weber et, K. Banaschek, Formänderung Und Profilrücknahme bei Gerad-und Schrägverzahnten, F. Vieweg und Sohn, Germany, 1953.
[9] A.Y. Attia, «Deflection of spur gear teeth cut in thin rims», J. Eng. Ind. 86 (4) (1964) 333-341.
[10] R.W. Cornell, «Compliance and stress sensitivity of spur gear teeth», J. Mech. Des. 103 (2) (1981) 447-459.
[11] P. Sainsot, P. Velex, et O. Duverger, «Contribution of gear body to tooth deflections—a new bidimensional analytical formula», J. Mech. Des. 126 (4) (2004) 748-752, juill.
[12] Z. Chen et, Y. Shao, «Dynamic simulation of spur gear with tooth root crack propagating along tooth width and crack depth», Eng. Fail. Anal. 18 (8) (2011) 2149-2164.
[13] Z. Chen, W. Zhai, Y. Shao, K. Wang, et G. Sun, «Analytical model for mesh stiffness calculation of spur gear pair with non-uniformly distributed tooth root crack», Eng. Fail. Anal. 66 (2016) 502-514.
[14] F. Chaari, T. Fakhfakh, et M. Haddar, «Analytical modelling of spur gear tooth crack and influence on gearmesh stiffness», Eur. J. Mech. A/Solids 28 (2009) 461-468.
[15] O.D. Mohammed, M. Rantatalo, J.-O. Aidanpää, «Improving mesh stiffness calculation of cracked gears for the purpose of vibration-based fault analysis», Eng. Fail. Anal. 34 (2013) 235-251.
[16] D.K. Tse et H.H. Lin, «Separation distance ans static transmission error of involute spur gears», Nashville, TN, 1992.
[17] H.H. Lin, J. Wang, F.B. Oswald, J.J. Coy, «Effect of extended tooth contact on the modeling of spur gear transmission», Gear Technol. (1994).
[18] A. Singh et D.R. Houser, «Analysis of off-line of action contact at the tips of gear teeth», Milwaukee, Wisconsin, 1994.
[19] N. Thibault, A. Bourdon, D. Remond, et D. Lecouvreur, «Dynamic model of a deep grooves ball bearing dedicated to the study of instantaneous angular speed of rotating assemblies», Tribol. Int. 174 (2022).
[20] C. Liu, D. Qin, T.C. Lim, et al., «Dynamic characteristics of the herringbone planetary gear set during the variable speed process», J. Sound. Vib. 333 (24) (2014).
[21] J.L. Gomez, I. Khelf, A. Bourdon, H. André, D. Rémond, «Angular modeling of a rotating machine in non-stationary conditions: application to monitoring bearing defects of wind turbines with instantaneous angular speed», Mech. Mach. Theory. 136 (2019) 27–51.
[22] A. Bourdon, «Modélisation Dynamique Globale des Boîtes de Vitesses Automobile», INSA, Lyon, France, 1997.
[23] B.J. Hamrock et W.J. Anderson, «Rolling-element bearings», NASA Reference Publication 1105, 1983.
[24] A. Palmgren, Les Roulements descriptions, théorie, Applications, SKF, Paris, 1967.
[25] G. Lundberg, «Elastische Berührung zweier Halbraüme», Forsh. Ing. Wes. 10 (5) (1939) 201-211.
[26] K.L. Johnson, Contact Mechanics, Cambridge University Press, 1985.
[27] Y. Benaïcha, J. Perret-Liaudet, J.-D. Beley, E. Rigaud, et F. Thouverez, «On a flexible multibody modelling approach using FE-based contact formulation for describing gear transmission error», Mech. Mach. Theory. 167 (2022).
[28] E. Rigaud, «Modelling and analysis of static transmission error. effect of wheel body deformation and interactions between adjacent loaded teeth», Paris, France, 1999, p. 1961-1972.
[29] Z. Sun, S. Chen, Z. Hu, et X. Tao, «Improved mesh stiffness calculation model of comprehensive modification gears considering actual manufacturing», Mech. Mach. Theory. 167 (2022).
[30] Q. Leclere, F. Girardin, et D. Remond, «An analysis of instantaneous angular speed measurement errors», Chartres, France, 2013, p. 1-11.
[31] H. André, «Precision of the IAS monitoring system based on the elapsed time method in the spectral domain», Mech. Syst. Signal. Process. (2013).
[32] B. Guilbert, «Hybrid Modular Models for the Dynamic Study of High-Speed Thin-Rimmed Webbed Gears», INSA, Lyon, France, 2017.
[33] X. Li, A. Bourdon, D. Remond, et S. Kœchlin, «Angular-based modeling of unbalanced magnetic pull for analyzing the dynamical behavior of a 3-phase introduction motor», J. Sound. Vib. 494 (2021).